Applied Catalysis B: Environmental 331 (2023) 122689

Contents lists available at ScienceDirect

Applied Catalysis B: Environmental

journal homepage: www.elsevier.com/locate/apcatb

Bimetal-organic layer-derived ultrathin lateral heterojunction with continuous semi-coherent interfaces for boosting photocatalytic CO_2 reduction

Fei-Fei Chen [a,1], Linghao Zhou [a,1], Chao Peng [b,1], Dantong Zhang [b], Lingyun Li [a,*], Dongfeng Xue [b,*], Yan Yu [a,*]

[a] Key Laboratory of Advanced Materials Technologies, International (HongKong Macao and Taiwan) Joint Laboratory on Advanced Materials Technologies, College of Materials Science and Engineering, Fuzhou University, Fuzhou 350108, PR China

[b] Multiscale Crystal Materials Research Center, Shenzhen Institute of Advanced Technology, Chinese Academy of Sciences, Shenzhen 518055, PR China

ARTICLE INFO

Keywords:
Metal-organic layer
Lateral heterojunction
Semi-coherent interface
CO_2 reduction
Photocatalysis

ABSTRACT

Current heterojunction photocatalysts suffer from sluggish charge transfer due to the discontinuous interfaces at an atomic level. Herein, we report a NiO–Co_3O_4 ultrathin lateral heterojunction using NiCo-based bimetal–organic layers as precursors. The atomic-resolution images display a unique continuous semi-coherent interface between NiO and Co_3O_4. The experimental results confirm that the continuous semi-coherent interfaces effectively expedite the electron transfer from NiO to Co_3O_4. Concomitantly, the electron transfer raises *d*-band center of Co_3O_4 in NiO–Co_3O_4 toward Fermi level, as revealed by the density functional theory calculations. As a result, the *COOH intermediate can be strongly bound on cobalt reactive centers. The successful modulation of charge transfer and intermediate binding by continuous semi-coherent interfaces leads to a remarkable gas yield of 22.67 mmol h^{-1} from photocatalytic CO_2 reduction over NiO–Co_3O_4. This work highlights the crucial roles of interface engineering in regulating carrier kinetics and surface reactions.

1. Introduction

The excessive CO_2 release has caused a series of environmental issues such as greenhouse effect [1]. The efficient artificial photosynthesis is therefore urgently needed to mitigate the CO_2 concentration [2]. Photocatalytic CO_2 reduction (PCR) utilizing sustainable solar light has emerged as an environmentally friendly and low-cost strategy. Particularly, the products from PCR (CO, CH_4, CH_3OH, etc.) can be used as chemical feedstock or fuels [3–5], which simultaneously mitigates the global energy crisis. However, the CO_2 molecules with a high bond energy of C=O (750 kJ mol^{-1}) are extremely thermodynamically stable, thereby leading to low efficiency of PCR. Two strategies have been proposed to promote PCR by: (1) suppressing electron–hole recombination and expediting charge transfer; and (2) controlling surface reactions by stabilizing intermediates, facilitating product desorption, or altering reaction pathways [6–8].

On the one hand, heterojunction engineering is effective to realize spatial separation and transfer of the photogenerated carriers [9]. Currently, heterojunctions with various configurations have been reported, in order to enhance interfacial contact and thus charge transfer, including two dimension (2D)/2D heterojunctions [10,11], hollow hierarchical heterojunctions [12–14], and core/shell heterojunctions [15,16]. However, the interfaces of these traditional heterojunctions are usually discontinuous at an atomic level, thereby compromising the charge transfer [17,18]. Recently, the lateral heterojunctions with low lattice misfits have been proposed to overcome the limitations of the traditional heterojunctions [17]. Their continuous interfaces at an atomic level could prolong carrier lifetime and increase electron density, thus enabling rapid electron transfer [19,20]. However, current preparation methods of the lateral heterojunctions usually required multiple exchanges of feedstock and reactors, which not only relied on the quality of preformed substrates to a great extent but inevitably increased processing procedures and times [21].

On the other hand, it was reported that the formation of *COOH from *CO_2 or the formation of *CO from *COOH could be rate-limiting steps for the CO-producing reaction [22–25]. Both these two processes highly

* Corresponding authors.
E-mail addresses: lilingyun@fzu.edu.cn (L. Li), df.xue@siat.ac.cn (D. Xue), yuyan@fzu.edu.cn (Y. Yu).

[1] These authors contributed equally to this work.

https://doi.org/10.1016/j.apcatb.2023.122689
Received 26 October 2022; Received in revised form 8 January 2023; Accepted 23 March 2023
Available online 24 March 2023
0926-3373/

rely on the stabilization of *COOH intermediate, emphasizing the significance of the binding strength of *COOH in photocatalytic CO_2 reduction. In this regard, the position of *d*-band center is a very useful descriptor for the binding strength of intermediates [26], as it indicates the interaction between *d* states of transition metals and valence states of adsorbates. Generally, the closer the *d*-band center is to Fermi Level, the stronger the binding of intermediates on catalytic sites is [27]. As such, modulating *d*-band center is promising to enhance the binding strength of *COOH and thus gain a high PCR efficiency. The key point in modulating *d*-band center is to optimize electronic structure of catalysts [28]. The reported methods include metal doping [29–31], defect engineering [32], alloying [33], strain engineering [34], and microenvironment control [35]. However, these methods are usually performed on the individual catalysts, and suffer from: (1) low structural stability due to metal leaching and catalyst aggregation [30]; and (2) serious recombination of electrons and holes. Modulating *d*-band center on multicomponent catalysts may provide a solution. For example, Su et al. [36] reported that the electron transfer from Ni to Ni_3N could modulate *d*-band center and thus intermediate binding energies in the hydrogen oxidation reaction.

Based on the above analysis, this work aims to develop a lateral heterojunction to simultaneously regulate charge transfer and *d*-band center. Briefly, a kind of NiO–Co_3O_4 lateral heterojunction with unique continuous semi-coherent interfaces is fabricated through facile pyrolysis of NiCo-based metal–organic layers (NiCo-MOLs). Experimental and theoretical results demonstrate that the continuous semi-coherent interfaces accelerate the electron transfer from NiO to Co_3O_4, and concomitantly raise *d*-band center of Co_3O_4 toward Fermi level. The *COOH intermediate can be therefore strongly bound on cobalt reactive centers, as confirmed by in situ diffuse reflectance infrared Fourier transform (DRIFT) spectra. As a result, the NiO–Co_3O_4 lateral heterojunction exhibits higher product yields of 22.67 mmol h^{-1} than the traditional heterojunctions with discontinuous interfaces and many other state-of-the-art counterparts.

2. Experimental section

2.1. Chemicals

Cobalt chloride hexahydrate ($CoCl_2 \cdot 6\ H_2O$), nickel chloride hexahydrate ($NiCl_2 \cdot 6\ H_2O$), cobalt nitrate hexahydrate ($Co(NO_3)_2 \cdot 6\ H_2O$), nickel nitrate hexahydrate ($Ni(NO_3)_2 \cdot 6\ H_2O$), melamine, ethylene glycol, nitric acid, triethylamine, urea, triethanolamine (TEOA), and acetonitrile (CH_3CN) were purchased from Sinopharm Chemical Reagent Co., Ltd. Benzenedicarboxylic acid (BDC), polyvinylpyrrolidone (PVP) and methanol were purchased from Shanghai Aladdin Biochemical Technology Co., Ltd. N,N-dimethylformamide (DMF) was purchased from Xilong Scientific. $[Ru(bpy)_2]Cl_2 \cdot 6\ H_2O$ (bpy = 2,2′-bipyridine) was purchased from Tokyo Chemical Industry Co., Ltd. All chemicals were used as received without further purification.

2.2. Sample preparation

The NiCo-MOLs were synthesized by the ultrasound-assisted method. BDC (0.75 mmol) was dissolved in a mixed solution of DMF (32 mL), ethanol (2 mL), and ultrapure water (2 mL) under ultrasonication. Then $NiCl_2 \cdot 6\ H_2O$ (0.375 mmol) and $CoCl_2 \cdot 6\ H_2O$ (0.375 mmol) were added and dissolved. Triethylamine (0.8 mL) was quickly injected into the as-obtained solution under magnetic stirring. Subsequently, this solution was subjected to ultrasonic treatment for 8 h (40 kHz). The product was collected by centrifugation, and washed with ethanol 5 times and then ultrapure water 5 times. Finally, the NiCo-MOLs were obtained through vacuum-assisted freeze-drying. The NiCo-MOLs with different molar ratios of Ni/Co were prepared by changing the ratios of $NiCl_2 \cdot 6\ H_2O$ and $CoCl_2 \cdot 6\ H_2O$. Besides, the Ni-MOLs or Co-MOLs were prepared by similar procedures except that $NiCl_2 \cdot 6\ H_2O$ (0.75 mmol) or $CoCl_2 \cdot 6\ H_2O$ (0.75 mmol) were used as sources.

The bulk NiCo-based metal-organic frameworks (NiCo-MOFs) were synthesized by the solvothermal reaction. BDC (0.75 mmol) was dissolved in a mixed solution of DMF (32 mL), ethanol (2 mL), and ultrapure water (2 mL) under ultrasonication. Then $NiCl_2 \cdot 6\ H_2O$ (0.375 mmol) and $CoCl_2 \cdot 6\ H_2O$ (0.375 mmol) were added and dissolved. The as-obtained solution was transferred to a Teflon-lined stainless-steel autoclave. The solvothermal temperature and time were 140 °C and 24 h, respectively. The product was collected by centrifugation, and washed with ethanol 5 times and then ultrapure water 5 times. Finally, the bulk NiCo-MOFs were obtained through vacuum-assisted freeze-drying.

The NiO–Co_3O_4 lateral heterojunction was prepared through one-step pyrolysis of NiCo-MOLs. The pyrolysis was performed in the muffle furnace at 500 °C for 1 h, with a heating rate of 1 °C min^{-1}. The NiO–Co_3O_4 samples with different molar ratios of Ni/Co were prepared using the NiCo-MOLs with different molar ratios of Ni/Co as precursors.

The single-phase NiO was prepared through one-step pyrolysis of Ni-MOLs. The pyrolysis was performed in the muffle furnace at 500 °C for 1 h, with a heating rate of 1 °C min^{-1}.

The single-phase Co_3O_4 was prepared through one-step pyrolysis of Co-MOLs. The pyrolysis was performed in the muffle furnace at 500 °C for 1 h, with a heating rate of 1 °C min^{-1}.

The NiO/Co_3O_4 heterojunction with discontinuous interfaces was prepared by physically mixing Ni-MOL-derived NiO and Co-MOL-derived Co_3O_4 with a molar ratio of 1:1.

The bulk NiO–Co_3O_4 lateral heterojunction was prepared through one-step pyrolysis of bulk NiCo-MOFs. The pyrolysis was performed in the muffle furnace at 500 °C for 1 h, with a heating rate of 1 °C min^{-1}.

The sample NiO/Co_3O_4 #1 was synthesized by the reported method [37]. $Ni(NO_3)_2 \cdot 6\ H_2O$ (1.7 mmol), $Co(NO_3)_2 \cdot 6\ H_2O$ (1.7 mmol), and PVP (0.5 g) were dissolved in a mixed solution of ultrapure water (5 mL) and methanol (43 mL). After magnetic stirring for 1 h, this solution was transferred to a Teflon-lined stainless-steel autoclave. The solvothermal temperature and time were 180 °C and 6 h, respectively. The product was collected by centrifugation, washed with ultrapure water 5 times and then ethanol 5 times, and finally dried at 60 °C in an oven. The NiO/Co_3O_4 #1 was obtained through one-step pyrolysis of the as-fabricated NiCo-containing precursors. The pyrolysis was performed in the muffle furnace at 500 °C for 1 h, with a heating rate of 1 °C min^{-1}.

The sample NiO/Co_3O_4 #2 was synthesized by the reported method [38]. Melamine (1.0 g) was dissolved in ethylene glycol (30 mL), after which an aqueous solution of HNO_3 (60 mL, 0.1 mol L^{-1}) was added. The product was washed with ethanol and dried at 60 °C for 12 h. The product, $NiCl_2 \cdot 6\ H_2O$ (0.2 mmol) and $CoCl_2 \cdot 6\ H_2O$ (0.2 mmol) were dissolved in ethanol (20 mL), respectively, and then ultrasonicated for 1 h. The resulting solutions were mixed and magnetic stirred for 1 h, and finally dried at 60 °C for 12 to obtain NiCo-containing precursors. The NiO/Co_3O_4 #2 was obtained through one-step pyrolysis of the as-fabricated NiCo-containing precursors. The pyrolysis was performed in the muffle furnace at 500 °C for 1 h, with a heating rate of 1 °C min^{-1}.

The sample NiO/Co_3O_4 #3 was synthesized by the reported method [39]. $NiCl_2 \cdot 6\ H_2O$ (0.75 mmol) and $CoCl_2 \cdot 6\ H_2O$ (0.75 mmol) were dissolved in ultrapure water (30 mL). After stirring for 30 min, urea (1.08 g) was added. This solution was transferred to a Teflon-lined stainless-steel autoclave. The solvothermal temperature and time were 120 °C and 9 h, respectively. The product was washed with ultrapure water 3 times and then ethanol 3 times, and finally dried at 60 °C in an oven. The NiO/Co_3O_4 #3 was obtained through one-step pyrolysis of the as-fabricated NiCo-containing precursors. The pyrolysis was performed in the muffle furnace at 500 °C for 1 h, with a heating rate of 1 °C min^{-1}.

2.3. Characterization

The crystal phases of samples were determined by X-ray diffraction on a diffractometer (Rigaku Miniflex II), with a scan rate of 0.01° s^{-1}.

The scanning electron microscopy (Carl Zeiss Supra 55) and transmission electron microscopy (JEOL JEM 2100) were used to observe the microstructure of samples. The high-angle annular dark field scanning transmission electron microscopy images were acquired on a spherical aberration corrected microscope (FEI Themis Z). The fast Fourier transformation (FFT) and inverse FFT patterns were obtained using DigitalMicrograph software. The thickness of $NiO–Co_3O_4$ was determined by atomic force microscopy (Hitachi AFM5500M). The surface compositions of samples were analyzed by X-ray photoelectron spectroscopy (Thermo ESCALAB 250) and Raman spectroscopy (Thermo DXR 2Xi). The element contents were determined by an inductively coupled plasma optical emission spectrometer (PerkinElmer Optima 8300). Ultraviolet–visible spectra were obtained on a spectrometer (PerkinElmer Lambda 950). The N_2 and CO_2 adsorption–desorption isotherms were obtained on a surface area and porosimetry analyzer (Micromeritics ASAP2460) at temperatures of 77 K and 298 K, respectively. *In situ* diffuse reflectance infrared Fourier transform spectra were obtained on a spectrometer (Nicolet 607) to monitor the intermediates of CO_2 reduction in real time. The CO_2/H_2O mixture gas was purged into the sample chamber. The signals were recorded when the sample was irradiated with a Xenon lamp for 0, 10, 20, 30, 40, 50, and 60 min

2.4. Photocatalytic CO_2 reduction testing

The photocatalytic CO_2 reduction testing was performed in a liquid phase. A 300 W Xenon lamp with a cutoff filter was used as a visible light source ($\lambda > 420$ nm). The output power of light was adjusted as 1.2 W by photoradiometer (Beijing Perfectlight PL-MW 2000). Catalysts (1 mg) and $[Ru(bpy)_3]Cl_2{\cdot}6\ H_2O$ (8 mg) were dispersed in a mixed solution of CH_3CN (3 mL), H_2O (2 mL) and TEOA (1 mL) in a quartz reactor. The reactor was alternately evacuated and purged with CO_2 3 times, and finally inflated with CO_2 for 30 min. The reaction temperature was controlled at 30 °C by a heater and circulating cooling water. The products from CO_2 reduction were identified and analyzed by gas chromatography (Agilent 7890B).

2.5. Photoelectrochemical measurements

Photoelectrochemical measurements were carried out in a standard three-electrode quartz cell, using Ag/AgCl as a reference electrode and Pt electrode as a counter electrode, respectively. The FTO glass was used as a working electrode, where a square region (0.25 cm^2) was coated with catalysts. The transient photocurrent was recorded on an electrochemical analyzer (CH Instruments CHI660E) under irradiation with a Xenon lamp ($\lambda > 420$ nm). A mixed solution of CH_3CN, H_2O, and TEOA (vol/vol = 3:2:1) containing $[Ru(bpy)_3]Cl_2{\cdot}6\ H_2O$ was used as an electrolyte. Electrochemical impedance spectra were measured on an electrochemical workstation (Princeton PARSTAT MC). An aqueous solution of 5 mM $K_3[Fe(CN)_6]$/5 mM $K_4[Fe(CN)_6]$/0.1 M KCl was used as an electrolyte. Mott-Schottky testing was performed in Na_2SO_4 solution (0.2 mol L^{-1}) on an electrochemical workstation (Princeton PARSTAT MC).

2.6. Computation detail

Density functional theory calculations were performed using Vienna ab-initio simulation package (VASP) with projector augmented wave (PAW) pseudopotentials. The Perdew−Burke−Ernzerh of exchange–correlation function was used and cutoff energy for the plane-wave basis was set to 450 eV. The k-point sampling was obtained from the Monkhorst−Pack scheme with a (4 ×4 ×1) mesh. The convergence criteria for energy and forces were set to 1×10^{-4} eV and 0.05 eV Å^{-1}, respectively. A DFT+U approach was adopted and the effective Hubbard U values of 6.9 and 3.7 eV were used to account for the localized D-electrons of Ni and Co, respectively.

3. Results and discussion

3.1. Design and characterization of $NiO–Co_3O_4$ lateral heterojunction

The material design is depicted in Fig. 1**a**. First, the NiCo-MOL precursor is fabricated with the assistance of sonication. The MOLs are ultrathin MOF nanosheets, as revealed by scanning electron microscopy (SEM) image (Fig. 1**b**). The ultrathin structure of NiCo-MOLs is responsible for the formation of ultrathin metal oxides after pyrolysis. When NiCo-MOLs are subjected to high temperature in air, the organics are decomposed, and Ni and Co ions are simultaneously oxidized into NiO and Co_3O_4, respectively. Benefiting from the periodic arrangement of Ni and Co atoms in the NiCo-MOL framework, the NiO and Co_3O_4 grow and connect with each other. More importantly, the theoretical $d_{(111)}$ of Co_3O_4 (0.467 nm) is approximately twice that of NiO (0.241 nm). As such, the periodic arrangement of Ni and Co atoms in NiCo-MOLs and suitable lattice mismatch between NiO and Co_3O_4 allow the formation of the $NiO–Co_3O_4$ lateral heterojunction.

The structural evolution from NiCo-MOLs to $NiO–Co_3O_4$ is studied by SEM and transmission electron microscopy (TEM). It is observed that the NiCo-MOL-derived sample after thermal treatment maintains the sheet-like morphology (Fig. 1**c**). A relatively rough surface suggests the collapse of NiCo-MOL framework after pyrolysis. The TEM image reveals that such a sheet is assembled by numerous homogeneous nanoparticles (Fig. 1**d**). These nanoparticles connect with each other without obvious agglomeration (Fig. S1). The uniform nanoparticles with excellent dispersion mainly stem from the ultrathin structure and periodic arrangement of atoms in NiCo-MOLs. The translucence of nanoparticles in the TEM images suggests the thin thickness. The thickness of the $NiO–Co_3O_4$ nanoparticles is determined to be ~4 nm by atomic force microscopy (AFM) image and height profile (Fig. 1**e**). It is generally recognized that the ultrathin structure of photocatalysts can promote charge separation and transfer due to the short transport pathway [40, 41]. As such, this special ultrathin nanoparticle-assembled sheet-like architecture is desirable for PCR considering the highly exposed reactive centers and fast carrier transport. The material design of this work highlights the uniqueness of bimetal-organic layers in preparing ultrathin lateral heterojunction.

The X-ray diffraction (XRD) pattern of the NiCo-MOL-derived sample is shown in Fig. 1**f**. Two sets of characteristic diffraction peaks are identified and indexed into NiO (JCPDS #47–1049) and Co_3O_4 (JCPDS #43–1003). Selected area electron diffraction (SAED) also supports the XRD results (Fig. 1**g**). The diffraction rings indicate the polycrystalline nature of sample. The energy dispersive spectroscopy (EDS) shows the signals of Ni, Co, and O elements (Fig. S2). The contents of Ni and Co in $NiO–Co_3O_4$ are determined to be 404.62 and 403.66 mg g^{-1} by inductively coupled plasma optical emission spectrometer (ICP-OES), as shown in Table S1. The Ni/Co ratio is close to the theoretical value.

To reveal the interfaces between NiO and Co_3O_4, high-resolution TEM (HRTEM) images are obtained. As shown in Fig. 2**a** and **b**, besides individual NiO and Co_3O_4 nanoparticles, the nanoparticles having two sets of lattice fringes are clearly observed. Surprisingly, there is no evident phase boundary between two sets of lattice fringes, indicating that the continuous interfaces are spontaneously created. The interplanar distances of these two sets of lattice fringes are measured to be ~0.477 and ~0.246 nm, respectively, corresponding to (111) and (111) facets of Co_3O_4 and NiO. This kind of interface is assigned to the semi-coherent interface [42,43]. The lattice misfit is determined to be ~3% (see details in Equation S1 in the Supporting Information). Such a semi-coherent interface is common all over the $NiO–Co_3O_4$ samples (Fig. 2**a** and **b**).

To gain a deep insight into the $NiO–Co_3O_4$ lateral heterojunction, fast Fourier transformation (FFT) and inverse FFT (IFFT) patterns are obtained [44]. The FFT patterns are acquired from the region I and II of Fig. 2**b**, respectively. The lattice fringes reveal that the region I and II correspond to Co_3O_4 and NiO, respectively. The elemental mapping is

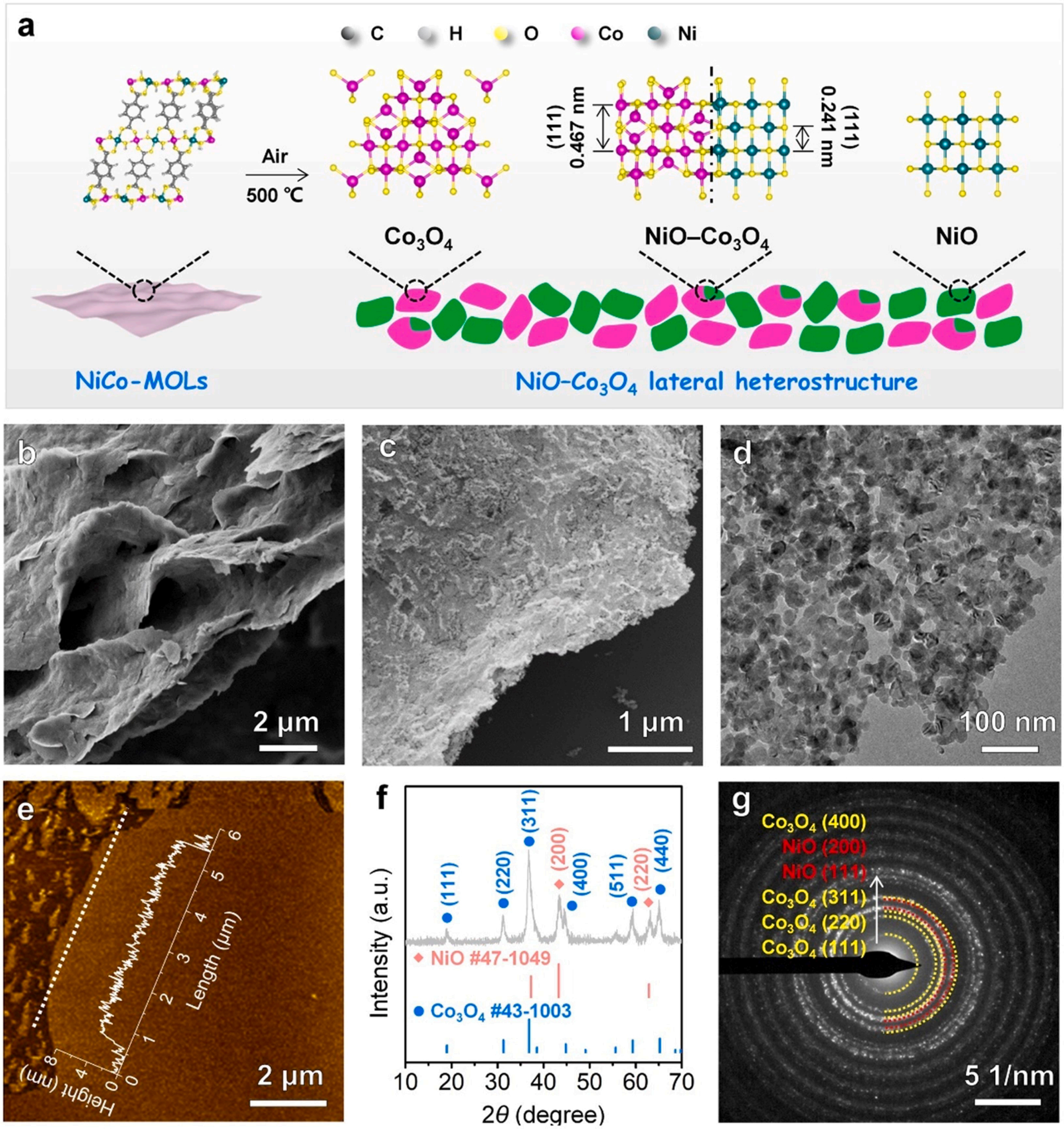

Fig. 1. (a) Schematic diagram of the NiO–Co_3O_4 lateral heterojunction. (b) SEM image of NiCo-MOLs. (c) SEM image, (d) TEM image, (e) AFM image and height profile, (f) XRD pattern, and (g) SAED of the NiO–Co_3O_4 lateral heterojunction.

useful to reveal the element distribution in the sample [45]. The elemental mapping of NiO–Co_3O_4 clearly displays the regions of Co_3O_4 and NiO (Fig. S3). The signals of Co_3O_4 and NiO are clearly observed and the corresponding facets are identified (Fig. 2**c** and **d**). The lattice distances determined from the linear profiles of IFFT patterns (Fig. S4) are identical to the results of HRTEM. It is shown that the $d_{(111)}$ of Co_3O_4 is almost double the $d_{(111)}$ of NiO, demonstrating the well-matched lattice parameters. Moreover, the IFFT patterns reveal that (111) plane of Co_3O_4 is almost parallel to that of NiO (Fig. 2**e** and **f**). These features ensure the formation of the continuous semi-coherent interfaces between NiO and Co_3O_4. The proportion of the continuous semi-coherent interfaces is hard to be estimated because some of NiO and Co_3O_4 nanoparticles are overlapped with each other (Fig. S3).

As shown in Fig. 2**g**, an individual NiO–Co_3O_4 particle with the continuous semi-coherent interfaces is clearly observed in high angle annular dark field scanning transmission electron microscopy (HAADF-STEM) image. The high transparency (marked by a white arrow) again supports the ultrathin structure of the NiO–Co_3O_4 nanoparticles. Furthermore, the atomic-resolution HAADF-STEM images were used to directly observe the interfaces at an atomic level. As shown in Fig. 2**h**, there are two kinds of regions having totally different atom arrangements in an individual NiO–Co_3O_4 particle. The region at the lower left

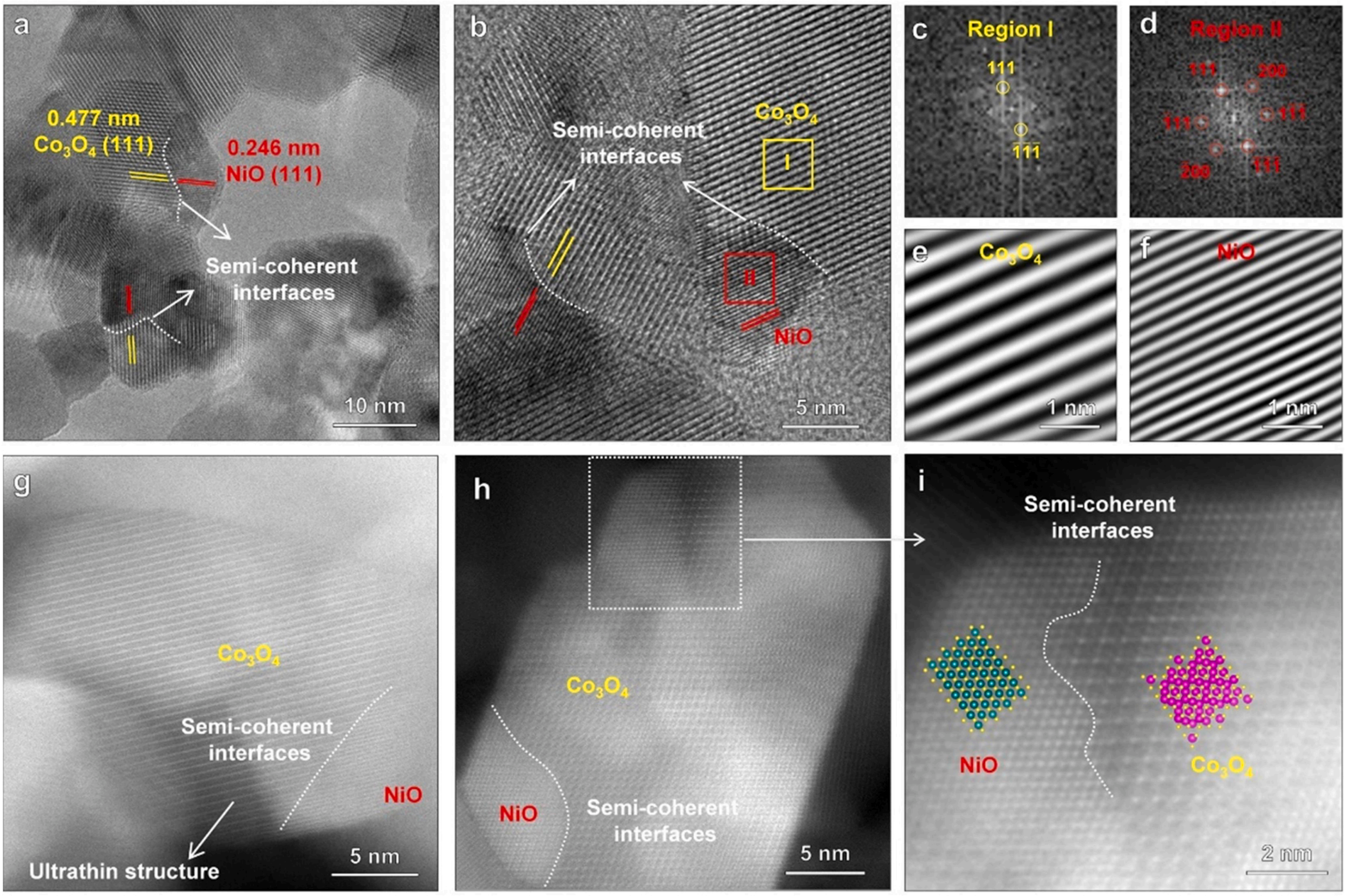

Fig. 2. (a, b) HRTEM, (c, d) FFT, (e, f) IFFT, and (g–i) HAADF–STEM images of the NiO–Co_3O_4 lateral heterojunction.

and upper left corners are assigned to NiO. The phase boundary between NiO and Co_3O_4 is not observed, corroborating the formation of the continuous interfaces at an atomic level. The enlarged HAADF-STEM image (Fig. 2**i**) reveals the regularly positioned dots. The atom arrangements of the left and right regions are in accord with the crystal structure of NiO and Co_3O_4, respectively, as illustrated by cell structure diagrams in the insets of Fig. 2**i**. These results confirm the successful preparation of a lateral heterojunction with the continuous semi-coherent interfaces.

To highlight the critical role of continuous semi-coherent interfaces in boosting catalytic activity of PCR, the pure NiO and Co_3O_4 are fabricated by similar methods (see details in the experimental section), using single-metal organic layers (i. e., Ni-MOLs and Co-MOLs) as precursors. The as-prepared NiO and Co_3O_4 also show similar sheet-like architecture (Fig. S5 and S6). The XRD and SAED patterns confirm the successful synthesis of single-phase NiO and Co_3O_4 (Fig. S7 and S8). In contrary to NiO–Co_3O_4, the nanoparticles with continuous interfaces are not found in the HRTEM images of NiO and Co_3O_4 (Fig. S9), highlighting the key role of bimetal organic layers in creating lateral heterojunctions. The contents of Ni and Co are determined to be 816.41 and 782.65 mg g^{-1} by ICP-OES, respectively, as recorded in Table S1. In addition, the physical mixture of NiO and Co_3O_4 is fabricated for comparison (labeled as NiO/Co_3O_4, see details in the experimental section). This NiO/Co_3O_4 sample can be considered as a traditional heterojunction given that it has similar components to NiO–Co_3O_4 but without continuous interfaces at an atomic level.

The influence of continuous semi-coherent interfaces on the physical and chemical properties of photocatalysts is further studied. The Raman spectra are shown in Fig. 3**a**. The Raman bands at around 1350 and 1590 cm^{-1}, corresponding to D-band and G-band of carbon [46,47], are absent for all samples, suggesting that organic ligands of MOLs are decomposed rather than transformed into carbon materials during pyrolysis. In the Raman spectrum of NiO, two Raman bands centered at 482 and 1062 cm^{-1} are assigned to longitudinal optical (LO) and 2LO phonon modes of NiO [48,49], respectively. In the Raman spectrum of Co_3O_4, five Raman bands are associated with $A_{1\,g}$ (680 cm^{-1}), $F_{2\,g}$ (613, 514, and 189 cm^{-1}), and E_g (479 cm^{-1}) modes of Co_3O_4 [50]. Among them, the signals of $A_{1\,g}$ (680 cm^{-1}) and $F_{2\,g}$ (189 cm^{-1}) stem from Raman vibrations of CoO_6 octahedral sites (i.e., Co^{3+}–O^{2-}) and CoO_4 tetrahedral sites (i.e., Co^{2+}–O^{2-}) [51], respectively. The Raman spectrum of NiO/Co_3O_4 shows similar Raman bands to that of NiO. The additional band at 686 cm^{-1} is assigned to $A_{1\,g}$ mode of Co_3O_4. The negligible shift of Raman bands suggests weak interaction between NiO and Co_3O_4 in the traditional heterojunction. In the Raman spectrum of NiO–Co_3O_4, the characteristic bands of NiO still keep almost unchanged. Two Raman bands at 189 and 646 cm^{-1} correspond to $F_{2\,g}$ and $A_{1\,g}$ modes of Co_3O_4, respectively. It is observed that the Raman band of $A_{1\,g}$ mode exhibits the big shift compared to the pure Co_3O_4. This change may result from that: (1) the continuous semi-coherent interfaces have a greater impact on Co_3O_4 than NiO; and (2) the particle size of NiO–Co_3O_4 is smaller than the pure NiO and Co_3O_4 [52], which is confirmed by the broadening of XRD peaks (Fig. S10). Since Ni and Co atoms are periodically arranged in NiCo-MOLs, the mutual confined growth between NiO and Co_3O_4 is responsible for the smaller particle sizes. The small-sized NiO–Co_3O_4 is expected to expose abundant active sites for accessibility of reactants and electrons. The increase in specific surface area of NiO–Co_3O_4 compared to the pure NiO and Co_3O_4 supports the result (Fig. S11).

The X-ray photoelectron spectroscopy (XPS) survey spectra show that both signals of Ni and Co are detected in the NiO/Co_3O_4 and

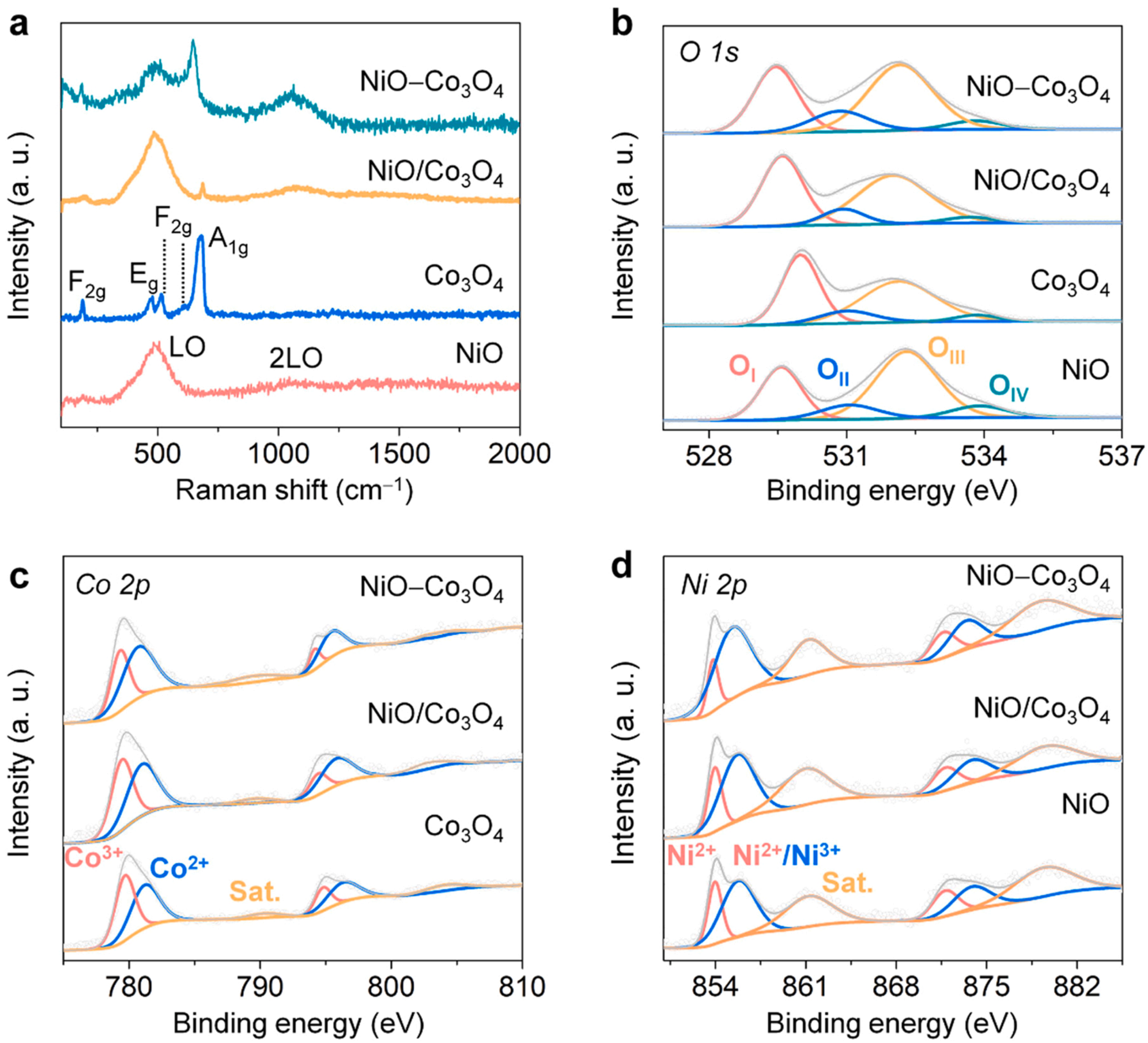

Fig. 3. (a) Raman spectra, (b) O 1 s, (c) Co 2p, and (d) Ni 2p XPS spectra of NiO, Co_3O_4, NiO/Co_3O_4, and NiO–Co_3O_4.

NiO–Co_3O_4 samples (Fig. S12). The XPS spectra of O 1 s, Co 2p, and Ni 2p are shown in Fig. 3**b–d**. In the O 1 s spectra, four kinds of oxygen species are identified, including lattice oxygen (O_I), surface-adsorbed oxygen or hydroxyl groups (O_{II} and O_{IV}), and oxygen vacancy (O_{III}) [53]. The concentration of oxygen vacancy (V_O) of four samples is listed in Table S2. The V_O concentration is highest for NiO and lowest for Co_3O_4. The V_O concentration of NiO/Co_3O_4 slightly increases compared to Co_3O_4 due to the introduction of NiO. The NiO–Co_3O_4 sample with similar components to NiO/Co_3O_4 shows a further increase in the V_O concentration, which is ascribed to semi-coherent interface-induced structural defects. It is deduced from Raman and XPS results that the oxygen atoms near Co atoms are more likely to be vacant in the NiO–Co_3O_4 lateral heterojunction. The previous study demonstrated that the catalytic sites with localized defects could trap the electrons, which elevated *d*-band center toward Fermi level [32]. As such, cobalt sites in NiO–Co_3O_4 are preferable to act as the reactive sites of PCR. The results of PCR testing, charge-transfer path, and theoretical calculations confirm this deduction (discussed later).

The electron transfer from NiO to Co_3O_4 in NiO–Co_3O_4 is confirmed by XPS spectra. The Co 2p spectra are shown in Fig. 3**c**. The peaks at around 779.8/794.9 and 781.3/796.5 eV are assigned to Co^{3+} and Co^{2+}, respectively [38,54]. The Ni 2p spectra are shown in Fig. 3**d**. The peaks at around 854.0/871.9 eV are assigned to the oxidation state of Ni^{2+} of NiO [55]. In addition, the peaks of around 855.9/874.1 eV are likely a mixture of Ni^{2+} of $Ni(OH)_2$ and Ni^{3+} of NiOOH [56,57]. This result suggests the presence of hydroxyl groups on the surface of NiO [58]. It is found that the content of Co^{2+} increases from Co_3O_4 to NiO/Co_3O_4 to NiO–Co_3O_4, along with a decrease in the content of Co^{3+} (Table S3). This result indicates that: (1) Co_3O_4 acquires electrons from NiO, resulting in a decrease in the valence state of Co species; (2) NiO–Co_3O_4 with the continuous interfaces shows a stronger interaction between NiO and Co_3O_4 than NiO/Co_3O_4 with discontinuous interfaces Table S3.

3.2. Photocatalytic CO_2 reduction testing

PCR, as a catalytic model, is employed to elucidate the superiority of the unique continuous semi-coherent interfaces in the catalytic processes. The photocatalytic testing is performed in a mixed liquid of CH_3CN, TEOA, and H_2O. The CH_3CN is used to enhance the dissolution of CO_2, the TEOA is a sacrifice agent to consume photogenerated holes and quench the excited photosensitizer, and H_2O is a proton source [59–61]. The photosensitizer $[Ru(bpy)_2]Cl_2{\cdot}6\ H_2O$ (labeled as **Ru**) is used to further amplify PCR efficiency [62,63]. In this work, CO and H_2 are main reduction products due to the thermodynamically favorable two-electron reactions [64–66]. The photocatalytic performance of NiO–Co_3O_4 is firstly optimized by adjusting pyrolysis temperature and Ni/Co ratios. The XRD patterns and gas yields of serial samples are shown in Fig. S13 and S14. The results show that the Ni/Co ratio of 1/1 and the pyrolysis temperature of 500 °C are the optimum experimental parameters. Therefore, the control samples discussed later are also

fabricated under the same conditions.

The roles of the NiO–Co_3O_4 lateral heterojunction in improving photocatalytic efficiency are highlighted by the following aspects:

(1) Heterojunction engineering is powerful to promote CO_2 reduction. As shown in Fig. 4**a**, the CO/H_2 generation rates over the pure NiO and Co_3O_4 are 2.73/0.16 and 9.32/3.71 mmol h^{-1}, with the CO selectivity of 94.46% and 71.52%, respectively. Wang et al. [67] demonstrated that free energy of H_2 evolution reaction on Ni sites was higher than that of Co sites, that was, H_2 evolution reaction could be effectively suppressed on Ni sites. This research result accounts for the high CO selectivity of NiO in this work. After building the lateral heterojunction, the CO/H_2 generation rates over NiO–Co_3O_4 are significantly increased to 16.15/6.52 mmol h^{-1}. The photocatalytic efficiency is improved by 7.84 and 1.74 times compared to the pure NiO and Co_3O_4, respectively. The CO selectivity of NiO–Co_3O_4 (71.24%) is close to that of Co_3O_4, probably because the reactive centers are maintained on cobalt sites in NiO–Co_3O_4.

(2) The continuous semi-coherent interfaces contribute to the efficient CO_2 reduction. As shown in Fig. 4**b** (left two columns), the NiO/Co_3O_4 heterojunction with discontinuous interfaces affords the CO/H_2 generate rates of 10.15/4.11 mmol h^{-1} (Fig. 4**b**), only displaying a slight increase relative to Co_3O_4. The photocatalytic efficiency of NiO/Co_3O_4 is considerably lower than that of NiO–Co_3O_4, even though they have identical components. To further emphasize the uniqueness of NiCo-MOL precursors in fabricating NiO–Co_3O_4 lateral heterojunction, different NiCo-containing precursors are synthesized and used as sources for fabricating NiO/Co_3O_4 heterojunctions, according to the reported works [37–39]. The NiO/Co_3O_4 #1, #2, and #3 samples are fabricated using polyvinylpyrrolidone (PVP) [37], melamine [38], and urea as raw materials [39] (see details in the Experimental Section). The XRD patterns of these NiO/Co_3O_4 samples are shown in Fig. S15. The presence of the characteristic peaks of NiO and Co_3O_4 indicates the successful fabrication of the NiO/-Co_3O_4 heterojunctions. However, no continuous interfaces are observed in these works [37–39], that is, these NiO/Co_3O_4

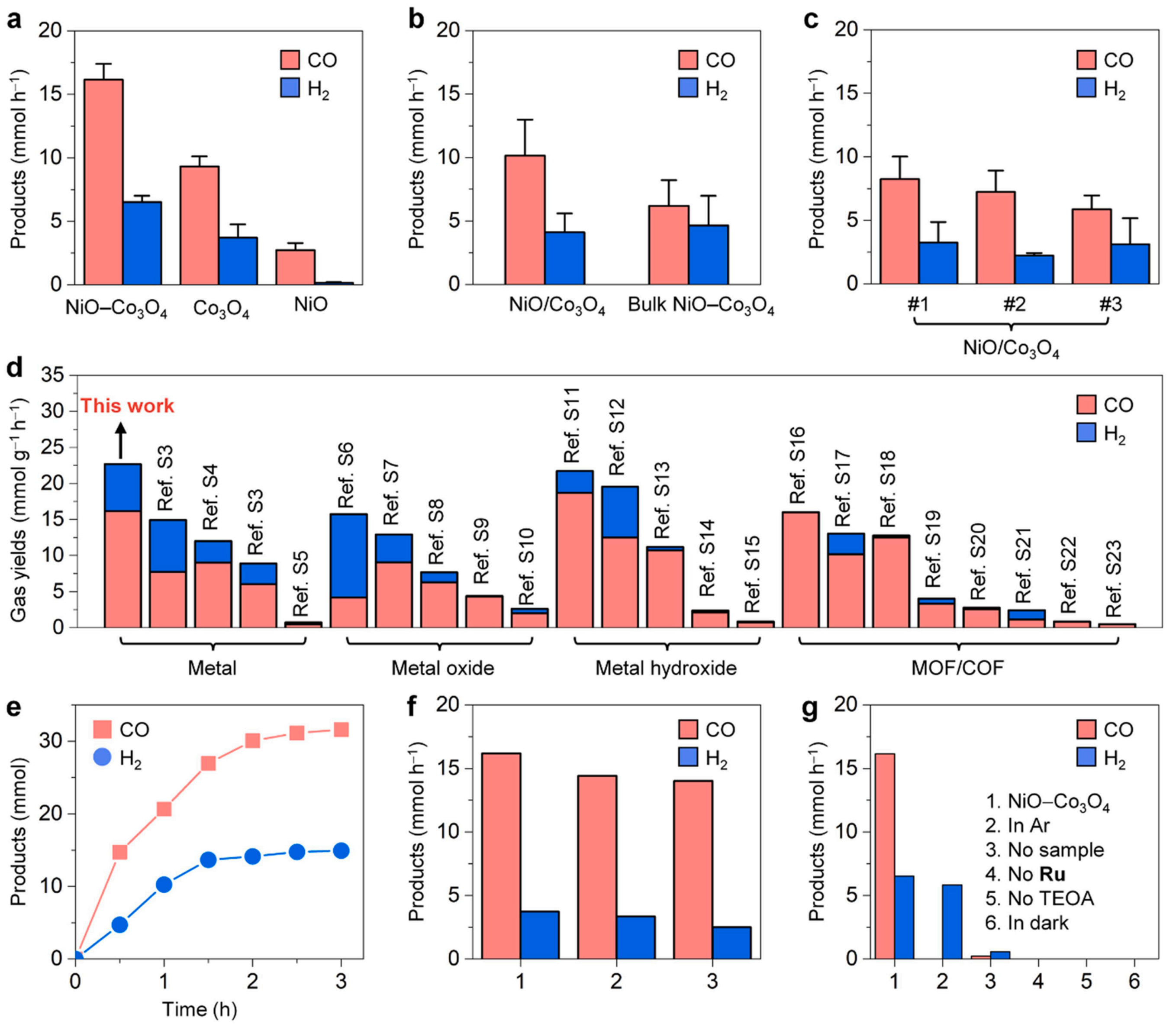

Fig. 4. (a–c) Gas generation rate over different samples. (d) Comparison of catalytic activities between NiO–Co_3O_4 and state-of-the-art catalysts. (e) Gas yields with time over NiO–Co_3O_4. (f) Gas generation rate during cycling testing of NiO–Co_3O_4. (g) Gas generation rate under different PCR conditions.

samples are traditional heterojunctions with discontinuous interfaces at an atomic level. As a result, it is expected that the NiO/Co_3O_4 #1, #2, and #3 samples suffer from sluggish charge transfer and thereafter inefficient CO_2 reduction, as shown in Fig. 4**c**. The results strongly highlight the unique advantage of NiCo-MOL precursors for the synthesis of lateral heterojunctions with continuous interfaces at an atomic level.

(3) The ultrathin structure with highly exposed active sites is also responsible for high gas yields. In order to verify this point, the bulk $NiO–Co_3O_4$ lateral heterojunction is fabricated using bulk NiCo-MOFs as precursors (see details in the Experimental Section). The bulk $NiO–Co_3O_4$ has similar XRD and SAED patterns to the ultrathin one (Fig. S16a and S16b). The HRTEM image of the bulk $NiO–Co_3O_4$ also displays the continuous semi-coherent interfaces (Fig. S16c). As shown in Fig. 4**b** (right two columns), the CO/H_2 yields (6.20/4.65 mmol h^{-1}) over the as-fabricated bulk $NiO–Co_3O_4$ lateral heterojunction are far less than that of the ultrathin one, probably because numerous reactive centers are confined in the interior of bulk $NiO–Co_3O_4$ and thus powerless for binding reactive molecules and accepting electrons.

The comparison between $NiO–Co_3O_4$ and state-of-the-art photocatalysts is provided in Fig. 4**d** and Table S4. The photocatalytic efficiency of the $NiO–Co_3O_4$ lateral heterojunction is comparable to or even significantly superior to that of state-of-the-art photocatalysts, including metals, metal oxides, metal hydroxides, and MOF/covalent organic framework (COF). The gas yield with time over $NiO–Co_3O_4$ is shown in Fig. 4**e**. The CO and H_2 are steadily generated in first two hours, after which the gas generation rate decreases. This decrease is mainly ascribed to the photobleaching of **Ru**. The result is consistent with the previous studies [59,68]. The accumulated CO/H_2 yields at time of 3 h are as high as 36.60/14.93 mmol. The cycling testing of $NiO–Co_3O_4$ exhibits a just slight decrease in gas generation rate after consecutive PCR for 3 times (Fig. 4**f**). The XRD and SAED patterns of sample after photocatalysis show the presence of NiO and Co_3O_4 (Fig. S17a and S17b), confirming that the crystal phases of $NiO–Co_3O_4$ keep almost unchanged. The sample after photocatalysis maintains the nanoparticle-assembled sheet-like architecture (Fig. S17c). In addition, the continuous semi-coherent interfaces can be still well identified (Fig. S17d). These results indicate the outstanding catalytic stability of $NiO–Co_3O_4$.

In addition, the effect of PCR conditions is studied by setting the control experiments. As shown in Fig. 4**g**, there is only H_2 generating under Ar atmosphere (column 2), verifying that CO comes from CO_2 reduction. A small amount of gas is generated without sample (column 3), suggesting that the photosensitizer **Ru** can reduce CO_2 to a certain degree. However, the gas yield is extremely low, the result of which highlights the significant roles of catalysts in binding CO_2 molecules and accelerating electron transfer. Nearly no gas can be detected in the absence of photosensitizer **Ru** and TEOA (column 4 and 5), suggesting that the gas yield under such a condition is below the detection limit of gas chromatography. This result demonstrate that the electrons produced by the cooperation between **Ru** and TEOA are powerful to promote PCR efficiency. The PCR is completely terminated in dark (column 6), verifying the light-driven processes. The phenomena of control experiments in this work are identical to the previous studies [69,70].

3.3. *Regulating charge transfer by continuous semi-coherent interfaces*

In order to track the intrinsic mechanism of enhanced PCR, a series of photoelectrochemical characterizations are performed. The band structure of $NiO–Co_3O_4$ is analyzed based on the results of Tauc and Mott-Schottky plots (see details in Fig. S18). The conduction band potentials of NiO and Co_3O_4 are estimated to be − 1.03 and − 0.65 eV (vs. Ag/AgCl), respectively. As such, the diagram of band structure of NiO and Co_3O_4 together with charge transfer pathway is shown in Fig. 5**a**. Under light irradiation, the electrons are excited to the conduction band, leaving the holes in the valence band. The holes in the valence bands of NiO and Co_3O_4 are consumed by TEOA, while the electrons in the conduction band of NiO are transferred to that of Co_3O_4. This process of

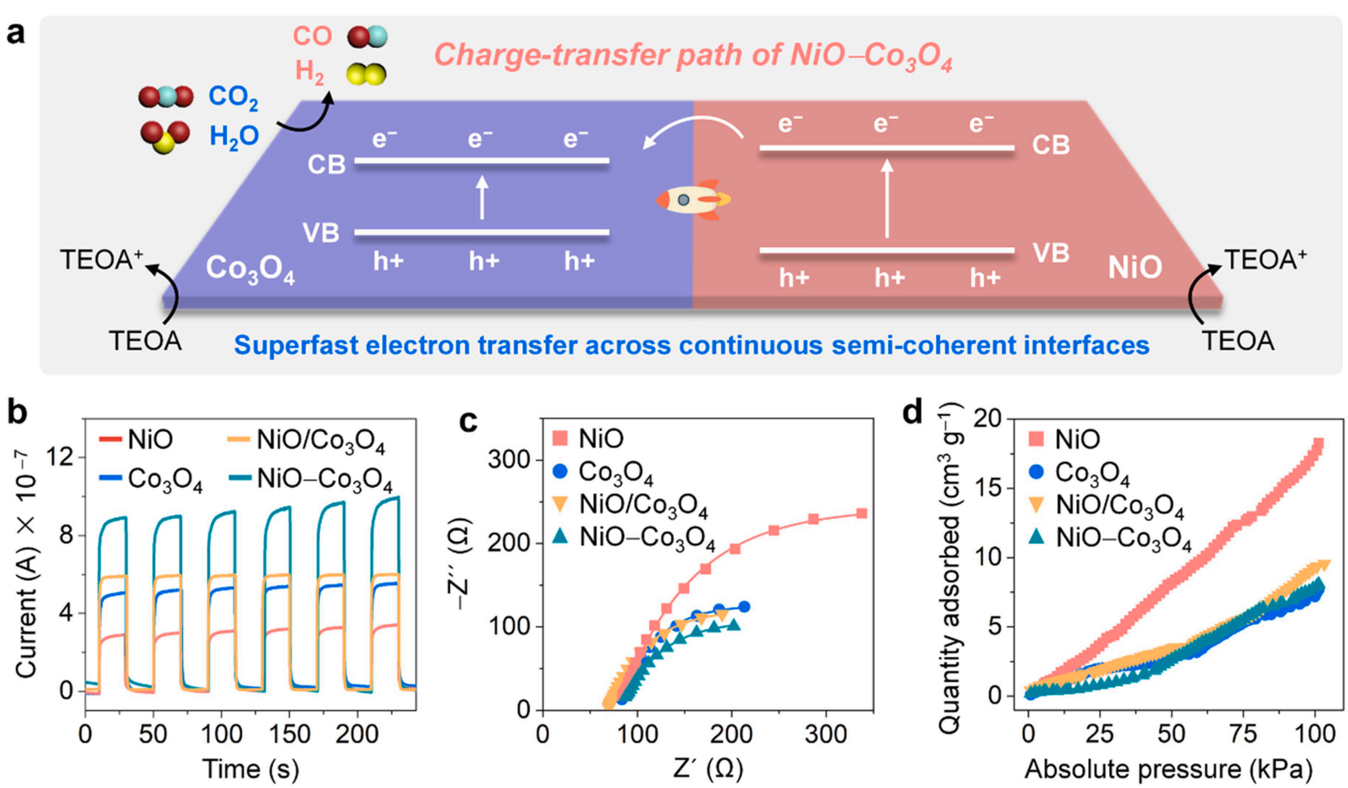

Fig. 5. (a) Proposed charge-transfer path of the $NiO–Co_3O_4$ lateral heterojunction. (b) Photocurrent response. (c) Nyquist plots. (d) CO_2 adsorption isotherms.

electron transfer is fast due to the continuous semi-coherent interfaces of NiO–Co_3O_4. Moreover, the photosensitizer **Ru** is used to further boost PCR, which is a common strategy reported elsewhere [62,63]. The photosensitizer $[Ru(bpy)_3]^{2+}$ can be excited to $[Ru(bpy)_3]^{2+*}$ and subsequently quenched by TEOA to generate a reduction state ($[Ru(bpy)3]^{+}$), after which electrons are transferred from $[Ru(bpy)3]^{+}$ to Co_3O_4 (Fig. S19). Eventually, the accumulated electrons in the conduction band of Co_3O_4 reduce CO_2 and H_2O into CO and H_2.

Among the above process, the efficiency of charge separation and transfer is evaluated by photocurrent response and electrochemical impedance spectroscopy (EIS). The photoelectrochemical results demonstrate that: (1) Co_3O_4 has a stronger ability of charge separation and transfer than NiO, as confirmed by the larger current across Co_3O_4 (Fig. 5**b**) and smaller semicircle radius of Nyquist plot (Fig. 5**c**); (2) the carrier kinetics of Co_3O_4 and NiO/Co_3O_4 is evenly matched, as confirmed by the comparable photocurrent response and the charge-transfer resistance. This result suggests that the traditional heterojunctions with discontinuous interfaces are hard to promote charge transfer and then improve photocatalytic efficiency compared to the individual component; and (3) the NiO–Co_3O_4 sample exhibits the largest current and smallest semicircle radius, reflecting the most powerful charge separation and transfer. This result emphasizes that the interface engineering is an effective route to mediate the carrier transport when the components of heterojunctions remain unchanged. The continuous interfaces seem to build a bridge between two components, and provide a smooth passage for carriers to rapidly pass. These photoelectrochemical results are highly consistent with that of PCR testing, reflecting the critical role of the carrier kinetics in adjusting the photocatalytic efficiency.

The CO_2 adsorption isotherms are shown in Fig. 5**d**. Among four samples, NiO displays the impressive adsorption quantity of CO_2 (18.27 cm^3 g^{-1}) compared to the other three samples, representing its powerful ability to adsorb CO_2 molecules. However, NiO with the largest adsorption amount of CO_2 exhibits the lowest photocatalytic efficiency. On the other hand, the NiO–Co_3O_4 sample with a moderate CO_2 uptake (8.10 cm^3 g^{-1}) shows the most efficient CO_2 reduction. The results suggest that CO_2 adsorption may not be a major contributor to the enhanced PCR in this work. The comparison of overall properties of NiO, Co_3O_4, NiO/Co_3O_4 and NiO–Co_3O_4 is summarized in Table S5.

3.4. *Regulating d-band center by continuous semi-coherent interfaces*

The surface reactions including CO_2 adsorption, activation, and conversion are also of great importance for efficient PCR. As such, the CO_2 reduction process on the surface of NiO–Co_3O_4 is studied by in situ DRIFT spectra. Generally, the CO molecules are produced from the transition state (*CO), which is generated by *COOH splitting. The formation of *COOH and *CO are verified by in situ DRIFT spectra. As shown in Fig. 6**a**, the signals of DRIFT spectra are recorded every 10 min. Before light irradiation (0 min), the absorption bands that are associated with intermediates of CO_2 reduction are not well identified. The DRIFT spectra recorded after light irradiation of 10–60 min clearly exhibit the presence of m-CO_3^{2-} (1506 and 1374 cm^{-1}), b-HCO_3^- (1457 cm^{-1}), and b-CO_3^{2-} (1339 cm^{-1}) [8]. The presence of these

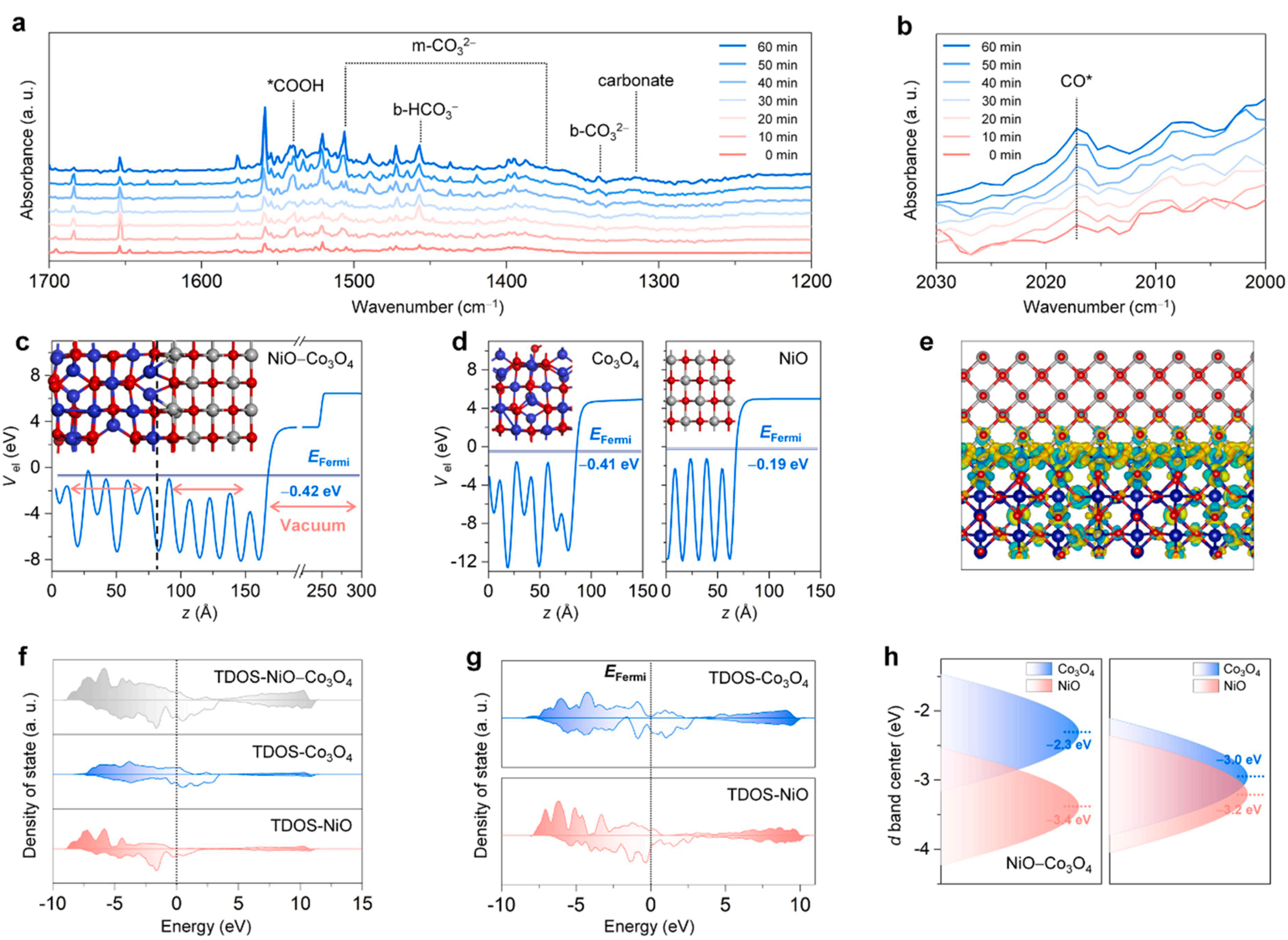

Fig. 6. (a, b) *In situ* DRIFT spectra of NiO–Co_3O_4. (c, d) Electrostatic potentials of NiO–Co_3O_4, Co_3O_4 and NiO. (e) Charge density difference of NiO–Co_3O_4. (f) Density of states of NiO–Co_3O_4. (g) Density of states of the pure Co_3O_4 and NiO systems. (h) The position of *d*-band center of NiO–Co_3O_4, Co_3O_4 and NiO.

species verifies the successful adsorption of CO_2 and H_2O molecules on the surface of samples [71]. These species does not participate in the CO_2 conversion. On the other hand, the characteristic absorption band of *COOH at 1540 cm^{-1} becomes much stronger over time, confirming the strong binding of *COOH on NiO–Co_3O_4. Simultaneously, the intensity of absorption band at 2017 cm^{-1}, which is assigned to *CO, is also gradually enhanced (Fig. 6**b**). On the other hand, the CO_2 fingerprint modes (3900–3500 cm^{-1}) display the attenuated absorption bands (Fig. S20). The results of in situ DRIFT spectra confirm the reaction pathways of *CO_2 → *COOH → *CO → CO [7], and strong binding of intermediates. In order to highlight the optimized binding of intermediates (*COOH and *CO) on the NiO–Co_3O_4 lateral heterojunction, in situ DRIFT spectra of the pure NiO and Co_3O_4 are measured, as shown in Fig. S21. There is no evident change in the signal intensity of *COOH and *CO for the pure NiO with time increasing (Fig. S21a and S21b). Moreover, the absorption bands of *COOH and *CO in the DRIFT spectra of the pure Co_3O_4 are just slightly stronger over time (Fig. S21c and S21d). These results indicate that the continuous semi-coherent interfaces of NiO–Co_3O_4 are capable to optimize the interactions between intermediates and catalyst surfaces.

To gain a deep insight into strong binding of intermediates of the NiO–Co_3O_4 lateral heterojunction, density functional theory (DFT) calculations are performed. Theoretical model shows the continuous semi-coherent interfaces of NiO–Co_3O_4 along the (111) lattice planes (Fig. S22). Adjusted from the vacuum energy (Fig. 6**c** and **d**), the Fermi level of NiO (−0.19 eV) is higher than that of Co_3O_4 (−0.41 eV). The Fermi level of the NiO–Co_3O_4 heterojunction is − 0.42 eV, which is quite close to that of independent Co_3O_4 system, indicating the electron transfer from NiO to Co_3O_4. The electrostatic potential (EP) calculations also provide evidence for this result that a higher EP is identified at Co_3O_4 in the heterojunction system, while a lower EP is found in the separated Co_3O_4 slab. The charge density difference plot demonstrates that the transferred charges mainly distribute at the interface of NiO–Co_3O_4 (Fig. 6**e**). The Bader charge analysis shows that the NiO slab donates 0.18 |e| to the Co_3O_4 slab, thereby generating an electron-efficient Co_3O_4 system. The total density of states (TDOSs) show that there is considerable electron density across Fermi level in the NiO–Co_3O_4 system, which behaves similarly to that of the separated Co_3O_4 (Fig. 6**f** and **g**). The electron-rich and active surface states at the Fermi level of Co_3O_4 slab endow its higher catalytic activity of PCR relative to the NiO slab. The theoretical calculations corroborate the fact that the continuous semi-coherent interfaces dramatically expedite the charge transfer from NiO to Co_3O_4 in the NiO–Co_3O_4 lateral heterojunction.

The rapid charge transfer is expected to cause the shift of *d*-band center and then affect the binding strength of intermediates. As shown in Fig. 6**h**, the calculation results show that the position of *d*-band center of Co_3O_4 is − 2.3 eV in the NiO–Co_3O_4 system, which is 0.7 eV higher than that of the individual Co_3O_4 slab (−3.0 eV). The upshift of *d*-band center toward Fermi level can powerfully optimize the interactions between intermediates and catalyst surfaces [30,33,35], thereby enhancing binding of *COOH. The result of theoretical calculation is consistent with that of in situ DRIFT spectra.

4. Conclusions

In summary, benefiting from periodical atom arrangement in NiCo-MOLs and suitable lattice mismatch, a NiO–Co_3O_4 ultrathin lateral heterojunction is successfully fabricated, and displays the unique continuous semi-coherent interfaces. The continuous semi-coherent interfaces at an atomic level build a smooth bridge for expediting electron transfer. After arriving at reactive centers of Co_3O_4, the electrons reduce CO_2 and H_2O into CO and H_2. Concomitantly, the fast electron transfer raises the D-band center toward Fermi level, thereby optimizing the *COOH binding. As a result, the efficient PCR is achieved over the NiO–Co_3O_4 lateral heterojunction. The material design reported in this work highlights the dual functions of the continuous semi-coherent interfaces in regulating charge transfer and D-band center.

CRediT authorship contribution statement

Fei-Fei Chen: Methodology, Formal analysis, Writing – original draft. **Linghao Zhou**: Methodology, Formal analysis. **Chao Peng**: Methodology, Formal analysis. **Dantong Zhang**: Formal analysis. **Lingyun Li**: Conceptualization, Supervision, Funding acquisition, Writing – review & editing. **Dongfeng Xue**: Conceptualization, Writing – review & editing. **Yan Yu**: Conceptualization, Supervision, Funding acquisition, Writing – review & editing.

Declaration of Competing Interest

The authors declare that they have no known competing financial interests or personal relationships that could have appeared to influence the work reported in this paper.

Data availability

Data will be made available on request.

Acknowledgments

The financial support by the National Key Research and Development Program of China (2020YFA0710303) and the National Natural Science Foundation of China (51972061, U1905215, 52072076) is greatly appreciated.

Appendix A. Supporting information

Supplementary data associated with this article can be found in the online version at doi:10.1016/j.apcatb.2023.122689.

References

[1] M. Meinshausen, N. Meinshausen, W. Hare, S.C.B. Raper, K. Frieler, R. Knutti, D. J. Frame, M.R. Allen, Greenhouse-gas emission targets for limiting global warming to 2 °C, Nature 458 (2009) 1158–1162.

[2] Z. Sun, N. Talreja, H. Tao, J. Texter, M. Muhler, J. Strunk, J. Chen, Catalysis of carbon dioxide photoreduction on nanosheets: fundamentals and challenges, Angew. Chem. Int. Ed. 57 (2018) 7610–7627.

[3] X. Li, J. Yu, M. Jaroniec, X. Chen, Cocatalysts for selective photoreduction of CO_2 into solar fuels, Chem. Rev. 119 (2019) 3962–4179.

[4] Y. Zhao, G.I.N. Waterhouse, G. Chen, X. Xiong, L.Z. Wu, C.H. Tung, T. Zhang, Two-dimensional-related catalytic materials for solar-driven conversion of CO_x into valuable chemical feedstocks, Chem. Soc. Rev. 48 (2019) 1972–2010.

[5] E. Gong, S. Ali, C.B. Hiragond, H.S. Kim, N.S. Powar, D. Kim, H. Kim, S.-I. In, Solar fuels: Research and development strategies to accelerate photocatalytic CO_2 conversion into hydrocarbon fuels, Energy Environ. Sci. 15 (2022) 880–937.

[6] X. Li, Y. Sun, J. Xu, Y. Shao, J. Wu, X. Xu, Y. Pan, H. Ju, J. Zhu, Y. Xie, Selective visible-light-driven photocatalytic CO_2 reduction to CH_4 mediated by atomically thin $CuIn_5S_8$ layers, Nat. Energy 4 (2019) 690–699.

[7] Y. Shi, J. Li, C. Mao, S. Liu, X. Wang, X. Liu, S. Zhao, X. Liu, Y. Huang, L. Zhang, Van der waals gap-rich BiOCl atomic layers realizing efficient, pure-water CO_2-to-CO photocatalysis, Nat. Commun. 12 (2021) 5923.

[8] Y. Shi, G. Zhan, H. Li, X. Wang, X. Liu, L. Shi, K. Wei, C. Ling, Z. Li, H. Wang, C. Mao, X. Liu, L. Zhang, Simultaneous manipulation of bulk excitons and surface defects for ultrastable and highly selective CO_2 photoreduction, Adv. Mater. 33 (2021), 2100143.

[9] P. Xia, S. Cao, B. Zhu, M. Liu, M. Shi, J. Yu, Y. Zhang, Designing a 0D/2D S-scheme heterojunction over polymeric carbon nitride for visible-light photocatalytic inactivation of bacteria, Angew. Chem. Int. Ed. 59 (2020) 5218–5225.

[10] J. Fu, Q. Xu, J. Low, C. Jiang, J. Yu, Ultrathin 2D/2D WO_3/g-C_3N_4 step-scheme H_2-production photocatalyst, Appl. Catal. B 243 (2019) 556–565.

[11] Y. Geng, D. Chen, N. Li, Q. Xu, H. Li, J. He, J. Lu, Z-scheme 2D/2D α-Fe_2O_3/g-C_3N_4 heterojunction for photocatalytic oxidation of nitric oxide, Appl. Catal. B 280 (2021), 119409.

[12] K. Chen, X. Wang, Q. Li, Y.-N. Feng, F.-F. Chen, Y. Yu, Spatial distribution of $ZnIn_2S_4$ nanosheets on g-C_3N_4 microtubes promotes photocatalytic CO_2 reduction, Chem. Eng. J. 418 (2021), 129476.

[13] S. Wang, B.Y. Guan, X.W.D. Lou, Construction of $ZnIn_2S_4$-In_2O_3 hierarchical tubular heterostructures for efficient CO_2 photoreduction, J. Am. Chem. Soc. 140 (2018) 5037–5040.

[14] H. Cao, Y. Yan, Y. Wang, F.-F. Chen, Y. Yu, Dual role of g-C_3N_4 microtubes in enhancing photocatalytic CO_2 reduction of Co_3O_4 nanoparticles, Carbon 201 (2023) 415–424.
[15] C. Bie, B. Zhu, F. Xu, L. Zhang, J. Yu, In situ grown monolayer N-doped graphene on CdS hollow spheres with seamless contact for photocatalytic CO_2 reduction, Adv. Mater. 31 (2019), 1902868.
[16] B. Qiu, Q. Zhu, M. Du, L. Fan, M. Xing, J. Zhang, Efficient solar light harvesting CdS/Co_9S_8 hollow cubes for Z-scheme photocatalytic water splitting, Angew. Chem. Int. Ed. 56 (2017) 2684–2688.
[17] J. Wang, Z. Li, H. Chen, G. Deng, X. Niu, Recent advances in 2D lateral heterostructures, Nano-Micro Lett. 11 (2019) 48.
[18] H. Shan, J. Qin, Y. Ding, H.M.K. Sari, X. Song, W. Liu, Y. Hao, J. Wang, C. Xie, J. Zhang, X. Li, Controllable heterojunctions with a semicoherent phase boundary boosting the potassium storage of $CoSe_2$/$FeSe_2$, Adv. Mater. 33 (2021), 2102471.
[19] J. Hou, S. Cao, Y. Sun, Y. Wu, F. Liang, Z. Lin, L. Sun, Atomically thin mesoporous In_2O_{3-x}/In_2S_3 lateral heterostructures enabling robust broadband-light photo-electrochemical water splitting, Adv. Energy Mater. 8 (2018), 1701114.
[20] L. Wang, X. Zhao, D. Lv, C. Liu, W. Lai, C. Sun, Z. Su, X. Xu, W. Hao, S.X. Dou, Y. Du, Promoted photocharge separation in 2D lateral epitaxial heterostructure for visible-light-driven CO_2 photoreduction, Adv. Mater. 32 (2020), 2004311.
[21] P.K. Sahoo, S. Memaran, Y. Xin, L. Balicas, H.R. Gutiérrez, One-pot growth of two-dimensional lateral heterostructures via sequential edge-epitaxy, Nature 553 (2018) 63–67.
[22] S. Vijay, W. Ju, S. Brückner, S.-C. Tsang, P. Strasser, K. Chan, Unified mechanistic understanding of CO_2 reduction to CO on transition metal and single atom catalysts, Nat. Catal. 4 (2021) 1024–1031.
[23] J. Di, C. Chen, C. Zhu, P. Song, M. Duan, J. Xiong, R. Long, M. Xu, L. Kang, S. Guo, S. Chen, H. Chen, Z. Chi, Y.-X. Weng, H. Li, L. Song, M. Wu, Q. Yan, S. Li, Z. Liu, Cobalt nitride as a novel cocatalyst to boost photocatalytic CO_2 reduction, Nano Energy 79 (2021), 105429.
[24] X. Jiao, X. Li, X. Jin, Y. Sun, J. Xu, L. Liang, H. Ju, J. Zhu, Y. Pan, W. Yan, Y. Lin, Y. Xie, Partially oxidized SnS_2 atomic layers achieving efficient visible-light-driven CO_2 reduction, J. Am. Chem. Soc. 139 (2017) 18044–18051.
[25] X. Zu, Y. Zhao, X. Li, R. Chen, W. Shao, Z. Wang, J. Hu, J. Zhu, Y. Pan, Y. Sun, Y. Xie, Ultrastable and efficient visible-light-driven CO_2 reduction triggered by regenerative oxygen-vacancies in $Bi_2O_2CO_3$ nanosheets, Angew. Chem. Int. Ed. 60 (2021) 13840–13846.
[26] J.K. Nørskov, F. Abild-Pedersen, F. Studt, T. Bligaard, Density functional theory in surface chemistry and catalysis, Proc. Natl. Acad. Sci. 108 (2011) 937–943.
[27] S. Jiao, X. Fu, H. Huang, Descriptors for the evaluation of electrocatalytic reactions: d-band theory and beyond, Adv. Funct. Mater. 32 (2022), 2107651.
[28] Z. Wang, J. Huang, L. Wang, Y. Liu, W. Liu, S. Zhao, Z.-Q. Liu, Cation-tuning induced d-band center modulation on Co-based spinel oxide for oxygen reduction/evolution reaction, Angew. Chem. Int. Ed. 61 (2022), e202114696.
[29] R. Wang, Z. Qiu, S. Wan, Y. Wang, Q. Liu, J. Ding, Q. Zhong, Insight into mechanism of divalent metal cations with different d-bands classification in layered double hydroxides for light-driven CO_2 reduction, Chem. Eng. J. 427 (2022), 130863.
[30] X. Cui, J. Wang, B. Liu, S. Ling, R. Long, Y. Xiong, Turning Au nanoclusters catalytically active for visible-light-driven CO_2 reduction through bridging ligands, J. Am. Chem. Soc. 140 (2018) 16514–16520.
[31] X. Xiong, Y. Zhao, R. Shi, W. Yin, Y. Zhao, G.I.N. Waterhouse, T. Zhang, Selective photocatalytic CO_2 reduction over Zn-based layered double hydroxides containing tri or tetravalent metals, Sci. Bull. 65 (2020) 987–994.
[32] S. Gong, Y. Niu, X. Teng, X. Liu, M. Xu, C. Xu, T.J. Meyer, Z. Chen, Visible light-driven, selective CO_2 reduction in water by In-doped Mo_2C based on defect engineering, Appl. Catal. B 310 (2022), 121333.
[33] R. Long, Y. Li, Y. Liu, S. Chen, X. Zheng, C. Gao, C. He, N. Chen, Z. Qi, L. Song, J. Jiang, J. Zhu, Y. Xiong, Isolation of Cu atoms in pd lattice: forming highly selective sites for photocatalytic conversion of CO_2 to CH_4, J. Am. Chem. Soc. 139 (2017) 4486–4492.
[34] X. Cai, F. Wang, R. Wang, Y. Xi, A. Wang, J. Wang, B. Teng, S. Bai, Synergism of surface strain and interfacial polarization on Pd@Au core–shell cocatalysts for highly efficient photocatalytic CO_2 reduction over TiO_2, J. Mater. Chem. A 8 (2020) 7350–7359.
[35] X.-Y. Dong, Y.-N. Si, Q.-Y. Wang, S. Wang, S.-Q. Zang, Integrating single atoms with different microenvironments into one porous organic polymer for efficient photocatalytic CO_2 reduction, Adv. Mater. 33 (2021), 2101568.
[36] L. Su, D. Gong, N. Yao, Y. Li, Z. Li, W. Luo, Modification of the intermediate binding energies on Ni/Ni_3N heterostructure for enhanced alkaline hydrogen oxidation reaction, Adv. Funct. Mater. 31 (2021), 2106156.
[37] K. Xu, R. Zou, W. Li, Y. Xue, G. Song, Q. Liu, X. Liu, J. Hu, Self-assembling hybrid NiO/Co_3O_4 ultrathin and mesoporous nanosheets into flower-like architectures for pseudocapacitance, J. Mater. Chem. A 1 (2013) 9107–9113.
[38] M. Tahir, L. Pan, R. Zhang, Y.-C. Wang, G. Shen, I. Aslam, M.A. Qadeer, N. Mahmood, W. Xu, L. Wang, X. Zhang, J.-J. Zou, High-valence-state NiO/Co_3O_4 nanoparticles on nitrogen-doped carbon for oxygen evolution at low overpotential, ACS Energy Lett. 2 (2017) 2177–2182.
[39] M. Manikandan, Y. Hu, K. Cai, J. Zhang, W. Zhang, M. Niu, D. Hua, J. Shang, X. Wang, Electrochemical performance of hydrothermally synthesized NiO/Co_3O_4 nanocomposites with different mass ratio, Mater. Lett. 283 (2021), 128849.
[40] Y. Xiao, G. Tian, W. Li, Y. Xie, B. Jiang, C. Tian, D. Zhao, H. Fu, Molecule self-assembly synthesis of porous few-layer carbon nitride for highly efficient photoredox catalysis, J. Am. Chem. Soc. 141 (2019) 2508–2515.
[41] Y. Qin, H. Li, J. Lu, Y. Feng, F. Meng, C. Ma, Y. Yan, M. Meng, Synergy between van der waals heterojunction and vacancy in $ZnIn_2S_4$/g-C_3N_4 2D/2D photocatalysts for enhanced photocatalytic hydrogen evolution, Appl. Catal. B 277 (2020), 119254.
[42] S. Xue, W. Huang, W. Lin, W. Xing, M. Shen, X. Ye, X. Liang, C. Yang, Y. Hou, Z. Yu, X. Wang, Interfacial engineering of lattice coherency at ZnO-ZnS photocatalytic heterojunctions, Chem. Catal. 2 (2022) 125–139.
[43] Z. Zhang, M. Wang, F. Wang, Plasma-assisted construction of CdO quantum dots/CdS semi-coherent interface for the photocatalytic bio-CO evolution, Chem. Catal. 2 (2022) 1394–1406.
[44] C. Yang, R. Shao, Q. Wang, T. Zhou, J. Lu, N. Jiang, P. Gao, W. Liu, Y. Yu, H. Zhou, Bulk and surface degradation in layered Ni-rich cathode for Li ions batteries: defect proliferation via chain reaction mechanism, Energy Storage Mater. 35 (2021) 62–69.
[45] F. Huang, X. Li, Z. Zhang, Z. Jiang, G. Wang, L. Li, Y. Yu, An ultra-stable Eu^{3+} doped yttrium coordination polymer with dual-function sensing for Cr(VI) and Fe (III) ions in aqueous solution, Chin. J. Struct. Chem. 41 (2022) 2204068–2204074.
[46] F.-F. Chen, Z.-H. Dai, Y.-N. Feng, Z.-C. Xiong, Y.-J. Zhu, Y. Yu, Customized cellulose fiber paper enabled by an in situ growth of ultralong hydroxyapatite nanowires, ACS Nano 15 (2021) 5355–5365.
[47] F.-F. Chen, J. Chen, Y.-N. Feng, L. Li, Y. Yu, Controlling metallic Co^0 in ZIF-67-derived N-C/Co composite catalysts for efficient photocatalytic CO_2 reduction, Sci. China Mater. 65 (2022) 413–421.
[48] W. Wang, Y. Liu, C. Xu, C. Zheng, G. Wang, Synthesis of NiO nanorods by a novel simple precursor thermal decomposition approach, Chem. Phys. Lett. 362 (2002) 119–122.
[49] G. Zhou, D.-W. Wang, L.-C. Yin, N. Li, F. Li, H.-M. Cheng, Oxygen bridges between NiO nanosheets and graphene for improvement of lithium storage, ACS Nano 6 (2012) 3214–3223.
[50] V.G. Hadjiev, M.N. Iliev, I.V. Vergilov, The raman spectra of Co_3O_4, J. Phys. C Solid State Phys. 21 (1988) L199–L201.
[51] Y. Lou, J. Ma, X. Cao, L. Wang, Q. Dai, Z. Zhao, Y. Cai, W. Zhan, Y. Guo, P. Hu, G. Lu, Y. Guo, Promoting effects of In_2O_3 on Co_3O_4 for CO oxidation: tuning O_2 activation and CO adsorption strength simultaneously, ACS Catal. 4 (2014) 4143–4152.
[52] G. Cheng, T. Kou, J. Zhang, C. Si, H. Gao, Z. Zhang, O_2^{2-}/O^- functionalized oxygen-deficient Co_3O_4 nanorods as high performance supercapacitor electrodes and electrocatalysts towards water splitting, Nano Energy 38 (2017) 155–166.
[53] J. Zhang, J. Qian, J. Ran, P. Xi, L. Yang, D. Gao, Engineering lower coordination atoms onto NiO/Co_3O_4 heterointerfaces for boosting oxygen evolution reactions, ACS Catal. 10 (2020) 12376–12384.
[54] S. Adhikari, S. Selvaraj, S.-H. Ji, D.-H. Kim, Encapsulation of Co_3O_4 nanocone arrays via ultrathin NiO for superior performance asymmetric supercapacitors, Small 16 (2020), 2005414.
[55] D. Koushik, M. Jošt, A. Dučinskas, C. Burgess, V. Zardetto, C. Weijtens, M. A. Verheijen, W.M.M. Kessels, S. Albrecht, M. Creatore, Plasma-assisted atomic layer deposition of nickel oxide as hole transport layer for hybrid perovskite solar cells, J. Mater. Chem. C 7 (2019) 12532–12543.
[56] K. Zhu, S.K. Frehan, G. Mul, A. Huijser, Dual role of surface hydroxyl groups in the photodynamics and performance of NiO-based photocathodes, J. Am. Chem. Soc. 144 (2022) 11010–11018.
[57] K. Han, T. Kreuger, B. Mei, G. Mul, Transient behavior of Ni@NiO_x functionalized $SrTiO_3$ in overall water splitting, ACS Catal. 7 (2017) 1610–1614.
[58] J. Kim, H.J. Park, C.P. Grigoropoulos, D. Lee, J. Jang, Solution-processed nickel oxide nanoparticles with NiOOH for hole injection layers of high-efficiency organic light-emitting diodes, Nanoscale 8 (2016) 17608–17615.
[59] S. Wang, B.Y. Guan, X.W. Lou, Rationally designed hierarchical N-doped carbon@$NiCo_2O_4$ double-shelled nanoboxes for enhanced visible light CO_2 reduction, Energy Environ. Sci. 11 (2018) 306–310.
[60] H. Liu, F. Zhang, H. Wang, J. Xue, Y. Guo, Q. Qian, G. Zhang, Oxygen vacancy engineered unsaturated coordination in cobalt carbonate hydroxide nanowires enables highly selective photocatalytic CO_2 reduction, Energy Environ. Sci. 14 (2021) 5339–5346.
[61] L. Chen, X. Wang, Y. Chen, Z. Zhuang, F.-F. Chen, Y.-J. Zhu, Y. Yu, Recycling heavy metals from wastewater for photocatalytic CO_2 reduction, Chem. Eng. J. 402 (2020), 125922.
[62] F. Xu, K. Meng, B. Cheng, S. Wang, J. Xu, J. Yu, Unique S-scheme heterojunctions in self-assembled TiO_2/$CsPbBr_3$ hybrids for CO_2 photoreduction, Nat. Commun. 11 (2020) 4613.
[63] L. Li, X. Dai, D.-L. Chen, Y. Zeng, Y. Hu, X.W. Lou, Steering catalytic activity and selectivity of CO_2 photoreduction to syngas with hydroxy-rich Cu_2S@R_{OH}-$NiCo_2O_3$ double-shelled nanoboxes, Angew. Chem. Int. Ed. 61 (2022), e202205839.
[64] X. Wang, J. Chen, Q. Li, L. Li, Z. Zhuang, F.-F. Chen, Y. Yu, Light-driven syngas production over defective $ZnIn_2S_4$ nanosheets, Chem. Eur. J. 27 (2021) 3786–3792.
[65] R. Zeng, K. Lian, B. Su, L. Lu, J. Lin, D. Tang, S. Lin, X. Wang, Versatile synthesis of hollow metal sulfides via reverse cation exchange reactions for photocatalytic CO_2 reduction, Angew. Chem. Int. Ed. 60 (2021) 25055–25062.
[66] J. Qin, S. Wang, X. Wang, Visible-light reduction CO_2 with dodecahedral zeolitic imidazolate framework ZIF-67 as an efficient co-catalyst, Appl. Catal. B 209 (2017) 476–482.
[67] X.-K. Wang, J. Liu, L. Zhang, L.-Z. Dong, S.-L. Li, Y.-H. Kan, D.-S. Li, Y.-Q. Lan, Monometallic catalytic models hosted in stable metal–organic frameworks for tunable CO_2 photoreduction, ACS Catal. 9 (2019) 1726–1732.
[68] X. Lin, Y. Gao, M. Jiang, Y. Zhang, Y. Hou, W. Dai, S. Wang, Z. Ding, Photocatalytic CO_2 reduction promoted by uniform perovskite hydroxide $CoSn(OH)_6$ nanocubes, Appl. Catal. B 224 (2018) 1009–1016.

[69] H. Zhong, R. Sa, H. Lv, S. Yang, D. Yuan, X. Wang, R. Wang, Covalent organic framework hosting metalloporphyrin-based carbon dots for visible-light-driven selective CO_2 reduction, Adv. Funct. Mater. 30 (2020), 2002654.

[70] L. Tan, S.-M. Xu, Z. Wang, Y. Xu, X. Wang, X. Hao, S. Bai, C. Ning, Y. Wang, W. Zhang, Y.K. Jo, S.-J. Hwang, X. Cao, X. Zheng, H. Yan, Y. Zhao, H. Duan, Y.-F. Song, Highly selective photoreduction of CO_2 with suppressing H_2 evolution over monolayer layered double hydroxide under irradiation above 600nm, Angew. Chem. Int. Ed. 58 (2019) 11860–11867.

[71] F. Xu, J. Zhang, B. Zhu, J. Yu, J. Xu, $CuInS_2$ sensitized TiO_2 hybrid nanofibers for improved photocatalytic CO_2 reduction, Appl. Catal. B 230 (2018) 194–202.